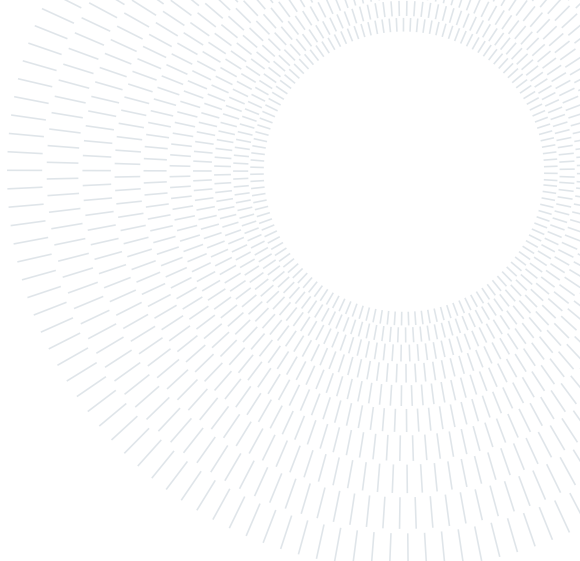




POLITECNICO
MILANO 1863

SCUOLA DI INGEGNERIA INDUSTRIALE
E DELL'INFORMAZIONE



Interplanetary trajectory design and planetary perturbations analysis

ORBITAL MECHANICS

Authors:

10723712	252142	MARCELLO PARESCHI	(BSc AEROSPACE ENGINEERING - POLITECNICO DI MILANO)
10836125	991195	DANIELE PATERNOSTER	(BSc AEROSPACE ENGINEERING - POLITECNICO DI MILANO)
10711624	249159	ALEX CRISTIAN TURCU	(BSc AEROSPACE ENGINEERING - POLITECNICO DI MILANO)
10884250	218180	TAMIM HARUN OR	(BSc AEROSPACE ENGINEERING - INTERNATIONAL ISLAMIC UNIVERSITY MALAYSIA)

Group ID: 2319

Professor: CAMILLA COLOMBO

Academic year: 2023-2024

Contents

Contents	1
1 Interplanetary mission	2
1.1 Introduction	2
1.1.1 Description of the problem	2
1.1.2 Assigned data and constraints	2
1.2 Algorithms description	2
1.2.1 Refined brute force algorithm	2
1.3 Reduction of the time windows	3
1.3.1 Resonance period analysis	3
1.3.2 Cost-plot analysis	4
1.4 Conclusion and results	6
1.4.1 Heliocentric legs	6
1.4.2 Gravity assist	7
2 Planetary mission	8
2.1 Introduction	8
2.1.1 Nominal Orbit	8
2.2 Groundtrack	8
2.2.1 Unperturbed Groundtrack	8
2.2.2 Perturbed Groundtrack	9
2.3 Orbit Propagation	11
2.3.1 History of the Keplerian Elements	11
2.3.2 Representation of the Evolution of the Orbit	13
2.3.3 Filtering	13
2.4 Comparison with Real Data	13
Bibliography	15

1. Interplanetary mission

1.1. Introduction

1.1.1. Description of the problem

The first part of the assignment aims at designing an interplanetary transfer from Mars to asteroid 1036 Ganymed exploiting a powered gravity assist on Earth. The problem is analyzed through the patched conics method, without considering the injection and arrival hyperbolae. The initial and final velocity vector of the satellite are assumed to be the same of the respective celestial body. The two heliocentric legs are calculated through the Lambert problem. The trajectory is selected with the only criteria of minimizing the cost of the mission, assessed through the total ΔV . The latter is computed by summing different contributions:

$$\Delta V_{tot} = \Delta V_1 + \Delta V_2 + \Delta V_3 \quad \Delta V_i = \|V_{+,i} - V_{-,i}\| \quad (1.1)$$

where $V_{-,i}$ and $V_{+,i}$ are the velocity vectors before and after the i -th manoeuvre respectively. The three terms are defined as:

- ΔV_1 related to the injection in the first heliocentric leg;
- ΔV_2 related to the exit from the second heliocentric leg;
- ΔV_3 related to the impulse given by the engine at pericentre of hyperbola fly-by;

All the manoeuvres are assumed to be impulsive, i.e. they change only the velocity vector of the spacecraft, maintaining invariated the position vector. Note that ΔV_1 and ΔV_2 are related to heliocentric velocities, while ΔV_3 is calculated through relative geocentric velocities.

1.1.2. Assigned data and constraints

A few constraints were considered:

- earliest departure date $t_{min,dep} = [01/01/2028 00 : 00 : 00]$ in Gregorian calendar
- latest arrival date $t_{max,arr} = [01/01/2058 00 : 00 : 00]$ in Gregorian calendar
- time of flights of the two heliocentric arcs must be greater than the associated parabolic time
- minimum pericentre radius of the fly-by hyperbola $r_p = r_E + 500 \text{ km}$
- single-revolution Lambert problem was considered
- reasonable total time of the mission

Note that the constraint on the pericentre radius of the fly-by is considered both for avoid impact on Earth and to prevent undesired atmospheric drag effects.

1.2. Algorithms description

The targeting problem previously defined can be seen as an optimization problem with three degrees of freedom (DOFs). Indeed, once the departing date and the two times of flight of the heliocentric legs are chosen, both the Lambert's arcs and the fly-by hyperbola are fully defined. Regarding the formulation of the Lambert's problem, it requires the knowledge of the initial and final position and also the imposed time of flight between them. For two Lambert's arcs it would be needed a total of six DOFs, but this quantities are dependant one to each other:

- the final position vector of the first arc corresponds to the initial position of the second one;
- the initial date for the departing on the second arc corresponds the arrival date on the first arc;
- fixing the first Lambert's arc, the final position and arrival date for the second Lambert's arc are related through the analytical ephemerides.

Once the two heliocentric legs are determined, the powered gravity assist follows as the geocentric velocity vectors are known.

The method implemented to solve the optimization problem is the **brute force algorithm** refined with the **gradient descent algorithm**. Then, to validate the results, the **brute force algorithm** has been used solely with a more dense search grid in a reasonable domain.

1.2.1. Refined brute force algorithm

The presented [Algorithm 1](#) is reliable, yet computationally demanding since the research of the minimum is performed through a triple-nested *for* loop. The time of the execution highly depends on the refinement chosen for the three selected periods of time. From this considerations and also noticing that the function to minimize presents

high irregularities, it is clear that narrow time windows can help in the overall research. Moreover, with this last observation, it is possible to use a less fine grid of research, since it is reasonable to think that the function will present less irregularities.

Algorithm 1 Brute-force algorithm

```

Require:  $T_{dep}, \Delta T_1, \Delta T_2$ 
 $\Delta V_{min} = 10^{10}$ 
for  $i$  in  $T_{dep}$  do
    for  $j$  in  $\Delta T_1$  do
        Calculate  $T_{fly-by}$ , first Lambert's arc, Mars' velocity at  $T_{dep}$  and  $\Delta V_1$ 
        for  $k$  in  $\Delta T_2$  do
            Calculate  $T_{arr}$ , second Lambert's arc, Asteroid's velocity at  $T_{arr}$ ,  $\Delta V_2, \Delta V_3, \Delta V_{tot}$ 
            if  $\Delta V_{tot} < \Delta V_{min}$  and  $r_p > r_{Earth} + 500 \text{ km}$  then
                 $\Delta v_{min} = \Delta V_{tot}$ 
                 $T_{dep,min} = T_{dep}; T_{fb,min} = T_{fb}; T_{arr,min} = T_{arr}$ 
            end if
        end for
    end for
end for
Minimize cost using  $fminunc$  with initial guess  $(T_{dep,min}; T_{fb,min}; T_{arr,min})$ 
return  $\Delta V_{min}; T_{dep,min}; T_{fb,min}; T_{arr,min}$ 
```

As a consequence, it was decided to perform a physical analysis (section 1.3) in order to wisely reduce the time domains for departure, fly-by and arrival. The idea of Algorithm 1 is that, once this reduction is performed, the brute-force search can be carried out on a small but refined grid. To speed up the process and refine the solution, $fminunc$ of MATLAB was used. The selected initial guess is the outcome of the brute force research.

In order to completely validate the results, the robustness of the brute force algorithm has been exploited. Referring to Algorithm 1, $fminunc$ was removed after the for-loop search and the research grid was refined. Moreover, with this computation it is possible to validate the time reduction analyzed in section 1.3.

1.3. Reduction of the time windows

1.3.1. Resonance period analysis

The first natural reduction on the domain of interest that could come to mind is to search the frequency on which the three celestial bodies repeat the relative positions on their orbits. On the approximation of circular orbits, this particular time period would be the synodic period generalized for the case of three bodies. However, this path is unviable because the orbit of the asteroid has a relevant eccentricity. To better comprehend the problem of having that eccentricity, particular attention have to be paid on the definitions of phasing and synodic period for two bodies:

- **Phasing ϕ** → the angle between two celestial bodies, calculated as the difference in their **true anomalies**:

$$\phi(t) = \theta^{(2)}(t) - \theta^{(1)}(t) \quad (1.2)$$

- **Synodic period T_{syn}** → if two celestial bodies have initial phasing ϕ_0 , they will return to the same phasing after a synodic period T_{syn} :

$$\phi(t_0) = \phi_0 \rightarrow \phi(t_0 + T_{syn}) = \phi_0 \quad (1.3)$$

As the definitions rely on the **true anomalies** of celestial bodies, non-circular orbits mean that the same phasing does NOT imply the same relative positions between them. In other words, once the synodic period has passed, the phasing of the three considered bodies keeps unchanged but it could result in a completely different relative positions with respect to the initial condition.

The problem needs to be reformulated. The goal is to find the period of time that elapses between a state of orbital positions of the bodies and the next occurrence of the same state. In literature, this particular period is called **period of orbital resonance** and it will be here indicated as T_{res} . Supposing that the orbits keep the other Keplerian elements unchanged during the revolution, the relation on true anomalies can be expressed as:

$$\begin{cases} \theta^{(1)}(t_0) = \theta_0^{(1)} \\ \theta^{(2)}(t_0) = \theta_0^{(2)} \\ \theta^{(3)}(t_0) = \theta_0^{(3)} \end{cases} \rightarrow \begin{cases} \theta^{(1)}(t_0 + T_{res}) = \theta_0^{(1)} \\ \theta^{(2)}(t_0 + T_{res}) = \theta_0^{(2)} \\ \theta^{(3)}(t_0 + T_{res}) = \theta_0^{(3)} \end{cases} \quad (1.4)$$

Since the true anomaly for an orbit repeats itself every orbital period T , it results:

$$\begin{cases} \theta_0^{(1)} = \theta^{(1)}(t_0 + iT^{(1)}) = \theta^{(1)}(t_0 + T_{res}) \\ \theta_0^{(2)} = \theta^{(2)}(t_0 + jT^{(2)}) = \theta^{(2)}(t_0 + T_{res}) \\ \theta_0^{(3)} = \theta^{(3)}(t_0 + kT^{(3)}) = \theta^{(3)}(t_0 + T_{res}) \end{cases} \rightarrow T_{res} = iT^{(1)} = jT^{(2)} = kT^{(3)} \quad (i, j, k \in \mathbb{N}) \quad (1.5)$$

As obtained in [Equation 1.5](#), the resonance period T_{res} must be a multiple of all the three orbital periods. To find three compatible natural numbers for i, j, k , the following procedure can be followed:

```

i = 1; j = i ·  $T^{(1)}/T^{(2)}$ ; k = i ·  $T^{(1)}/T^{(3)}$ 
while j  $\notin \mathbb{N}$  or k  $\notin \mathbb{N}$  do           ▷ a tolerance tol must be implemented
    i = i + 1
    j = i ·  $T^{(1)}/T^{(2)}$ 
    k = i ·  $T^{(1)}/T^{(3)}$ 
end while
return i, j, k
```

Note that, since a perfect resonance of three celestial bodies is realistically impossible, a certain tolerance *tol* must be introduced when evaluating $j, k \in \mathbb{N}$ in order to compute a reasonable T_{res} . In the specific case of this report, the execution of the above algorithm returned the following results:

<i>tol</i>	<i>i</i> (Earth)	<i>j</i> (Mars)	<i>k</i> (1036 Ganymed)
0.1159	13	6.9119	4.8841

[Table 1.1](#): Results of the resonance analysis

T_{res} results to be 13 Earth's sidereal years, so the time domain can be restricted accordingly. It is important to keep in mind that this is an approximation, but since the mission has to depart in a reasonable date, it is acceptable to restrain the time window to the first 13 years. In any case, the cost of the mission will repeat similarly after 13 years.

1.3.2. Cost-plot analysis

The reduction of the departure time window in [subsection 1.3.1](#) is a powerful but not sufficient restriction for the domain to analyze with [Algorithm 1](#). Hence, a more detailed analysis has to be performed, including some restrictions for the first and second time of flight. The present paragraph presents and studies in detail two cost-plots. The first is related to the injection cost on the first Lambert's arc while the second exit cost is referred to the second Lambert's arc. Notice that the pork-chop plot of each leg can't be plotted, since the the two arcs are linked at the fly-by position. Given this consideration, the two cost plot obtained with the 13-year constrained departure window are following.

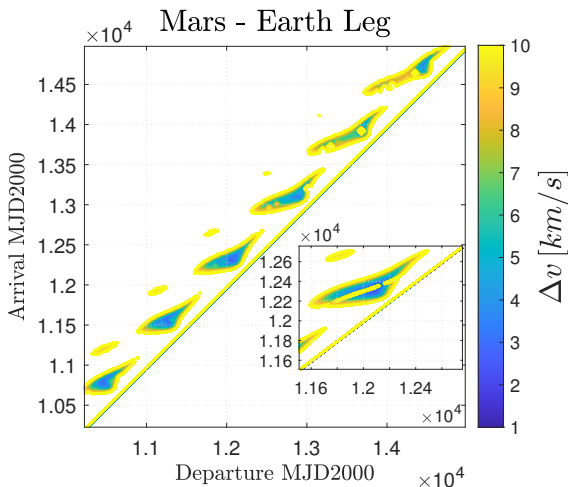


[Figure 1.1](#): Cost plot for 1st leg

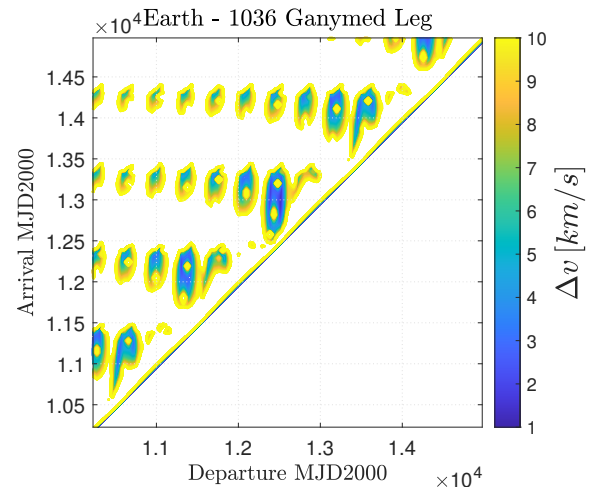


[Figure 1.2](#): Cost plot for 2nd leg

The contour plot are set to a maximum value for the ΔV of 10 km/s, greater values are excluded since they wouldn't be relevant for the present study. Moreover, it was decided to use symmetrical time domains for departure and arrival, expressed in $mjd2000$ units. Some important information can be retrieved from the contour plot of Figure 1.1.

- All the local minima that reach the lowest values are located along the diagonal, indicating that there is a constraint on the time of flight for the first arc. This behaviour is present also in the second arc Figure 1.2. Above the diagonal of both the plots the minima are higher Figure 1.2, or not existent Figure 1.1 for the set of contour lines considered. This is related to the fact that the Lambert's arc were calculated without considering the multi-revolution solutions subsection 1.1.2. Indeed, if the time of flight imposed is higher, the Lambert's arc solution will have a higher semi-major axis. This results in a higher ΔV to inject or exit the transfer arc since the energy difference between orbits becomes considerable. The solution that embraces multi-revolution arcs would benefit in this sense and could open new scenarios for the interplanetary arcs, as cited in^[1].
- It can be noticed that a repetition pattern of the minima is present in both the figures. With particular emphasis on the Mars-Earth leg, the minimum shown as the blue-coloured zone, repeats every synodic period Table 1.2. This is due to the quasi-circular orbits of both the planets.
- A repetition pattern is noticeable also in Figure 1.2. To better analyze the plot, the values of the last three columns of Table 1.2 can be exploited. It can be noticed that the synodic period $T_{syn}^{E,G}$ can not explain the reoccurrence of the minima while the resonance periods are both meaningful. The high tolerance resonance period $T_{res,1}^{E,G}$ fits all the repeated minima along the diagonal. The low tolerance resonance period $T_{res,2}^{E,G}$ can catch a lower frequency pattern, appreciable by focusing on the first and second-last *P-shaped* minima along the diagonal.
- Regarding the cost-plot of Earth-to-Mars transfer Figure 1.1, a particular behaviour of the minimum can be noticed on the zoomed box. The focus allows to appreciate a yellow ridge that separates the minimum zone in to two sub-area that contains mainly two minimum zones. As mentioned in^[1], the two zones correspond to two solutions for the Lambert's problem, in particular to the value of the transfer angle $\Delta\theta$. The upper zone is related to $\Delta\theta > \pi$ while the lower zone corresponds to $\Delta\theta < \pi$. When $\Delta\theta = \pi$, since the orbital planes of Earth and Mars are not exactly coincident, the plane of the heliocentric transfer leg becomes almost perpendicular to the ecliptic, increasing the injection cost of the mission^[2]. When the co-planar and the circular assumptions on Earth and Mars orbits are made, the central part of the minimum lobe in the zoomed box coincides with the Hohmann transfer^[1].

$T_{syn}^{M,E} [mjd2000]$	$T_{syn}^{E,G} [mjd2000]$	$T_{res,1}^{E,G}$ (high tol) [$mjd2000$]	$T_{res,2}^{E,G}$ (low tol) [$mjd2000$]
779.9418	585.0697	1095.7711	2922.0562

Table 1.2: Results of the resonance analysis

From the observations presented above, it was decided to analyze the same cost graph but plotting the time of flight on the y-axis. In order to consider reasonable time of flight domains, some coarse reduction was adopted. In particular, long times of flight are excluded for the already mentioned reasons, while very short times of flight are not taken into the domain since they are associated to high transfer-costs. Infact, this last situation corresponds to the yellow diagonal line of the plots in Figure 1.1 and Figure 1.2.

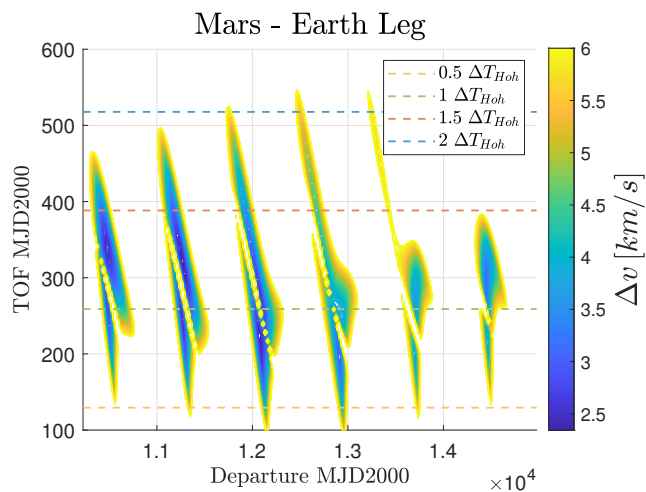


Figure 1.3: Cost plot for 1st leg

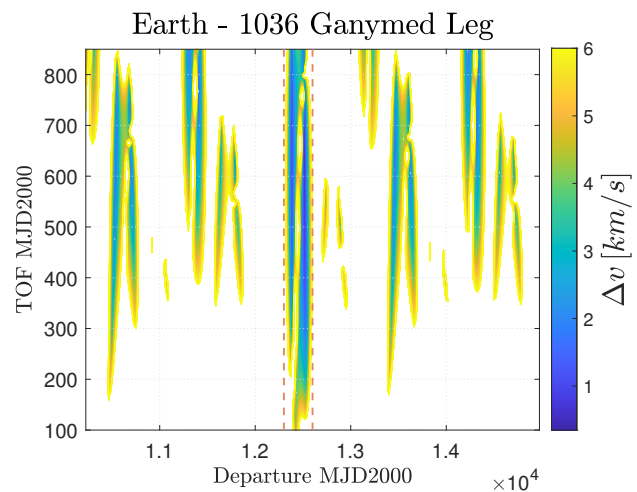


Figure 1.4: Cost plot for 2nd leg

For the Earth-Mars transfer, multiples and sub-multiples of the Hohmann transfer time were considered. The hypothesis is reasonable since Mars and Earth have almost circular and co-planar orbits^[3].

The same hypothesis can't be applied on the second heliocentric leg because of Ganymed's eccentric orbit and Hohmann's hypothesis doesn't hold. A relevant area of lowest minima can be noticed in Figure 1.4, in particular the vertical bar in the narrow of the fly-by date $1.25 \cdot 10^4 \text{ mjd2000}$. This means that by choosing this flyby date, the choice of the second time of flight is less relevant since the minima develops along all the plotted vertical. In addition to this, the Hohmann's time of flight multiples and submultiples can be considered for the first time of flight by subtracting them to the considered fly-by date. This operation generates a resized domain for the departure dates. Summing up all the considerations, the following restricted time domain was selected:

- $T_{dep} = 1.25 \cdot 10^4 - [0.65, 2] \cdot \Delta T_{Hoh} \text{ mjd2000}$
- $\Delta T_1 = [0.65, 2] \cdot \Delta T_{Hoh} \text{ mjd2000}$
- $\Delta T_2 = [200, 800] \text{ mjd2000}$

1.4. Conclusion and results

It was then used Algorithm 1 in the time domain selected at the end of subsection 1.3.2, using 40 elements for each array. The obtained results in terms of cost and dates are reported in the following tables:

$\Delta V_1 [\text{km/s}]$	$\Delta V_2 [\text{km/s}]$	$\Delta V_3 [\text{km/s}]$	$\Delta V_{tot} [\text{km/s}]$
4.0813	3.3130	$2.8919 \cdot 10^{-6}$	7.3942

Table 1.3: Costs ΔV of the optimal mission

Dep. Date	Fb. Date	Arr. Date	$\text{TOF}_{tot} (\text{yrs})$
[03/06/2033]	[10/02/2034]	[27/03/2036]	2.8146

Table 1.4: Optimal mission dates in Gregorian calendar

The obtained results were validated through the pure brute-force algorithm, with a grid of search in the 13 years reduced domain. In particular 100 elements where considered, the data obtained were:

$\Delta V_1 [\text{km/s}]$	$\Delta V_2 [\text{km/s}]$	$\Delta V_3 [\text{km/s}]$	$\Delta V_{tot} [\text{km/s}]$
4.5786	2.1223	1.0347	7.7357

Table 1.5: Costs validation

Dep. Date	Fb. Date	Arr. Date	$\text{TOF}_{tot} (\text{yrs})$
[07/07/2033]	[04/03/2034]	[23/03/2035]	1.7073

Table 1.6: Mission dates validation

1.4.1. Heliocentric legs

The two heliocentric legs associated with the solution computed through Algorithm 1 can be characterized through the keplerian elements shown in Table 1.7:

Arc	$a [\text{AU}]$	$e [-]$	$i [\text{deg}]$	$\Omega [\text{deg}]$	$\omega [\text{deg}]$	$\theta_{dep} [\text{deg}]$	$\theta_{arr} [\text{deg}]$
M→E	1.1602	0.2870	1.18	321.54	105.98	195.38	74.02
E→G	1.9445	0.5029	4.17	141.54	339.92	20.09	231.36

Table 1.7: Heliocentric legs

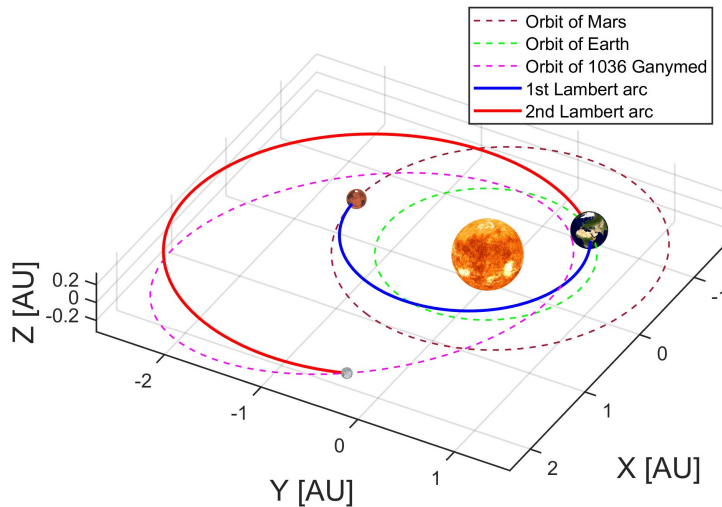


Figure 1.5: Optimal transfer trajectory - planet's dimension not in scale

The two heliocentric legs are displayed in Figure 1.5. The represented positions of Mars, Earth and 1036 Ganymed are respectively at departure, fly-by and arrival. All the orbits are plotted in the Heliocentric ecliptic inertial frame.

1.4.2. Gravity assist

Known the incoming and outgoing heliocentric velocities of the spacecraft and the Earth's velocity at the fly-by date, it was possible to completely characterize the two branches of hyperbola in an Earth-centred ecliptic frame. The main parameters of the hyperbola are reported in Table 1.8:

r_p [km]	δ_{tot} [deg]	v_∞^- [km/s]	v_∞^+ [km/s]	e_- [-]	e_+ [-]	ΔT_{soi} [h]	ΔV_{helio} [km/s]
7762.47	54.8918	7.743345	7.743341	2.167669	2.167667	64.4900	7.1386

Table 1.8: Gravity assist data

It can be noticed that the fly-by hyperbola respect the constraint on the pericentre radius given in subsection 1.1.2. Moreover, the impulse given by the engine at the pericentre (Table 1.3) is negligible with respect to the heliocentric fly-by manoeuvre cost, calculated as $\Delta V_{helio} = \|V_\infty^+ - V_\infty^-\|$. This confirms the efficiency effect of the examined fly-by. The permanence time passed inside the sphere of influence has been computed using the hyperbolic time law. In particular, considering the intersection between the two hyperbolic arcs and the radius of the Earth's sphere of influence (Equation 1.6), the true anomalies at entry and exit of SOI are computed.

$$r_{SOI,E} = r_{S \rightarrow E} \left(\frac{M_E}{M_S} \right)^{2/5} = 9.24647 \cdot 10^5 \text{ km} \quad (1.6)$$

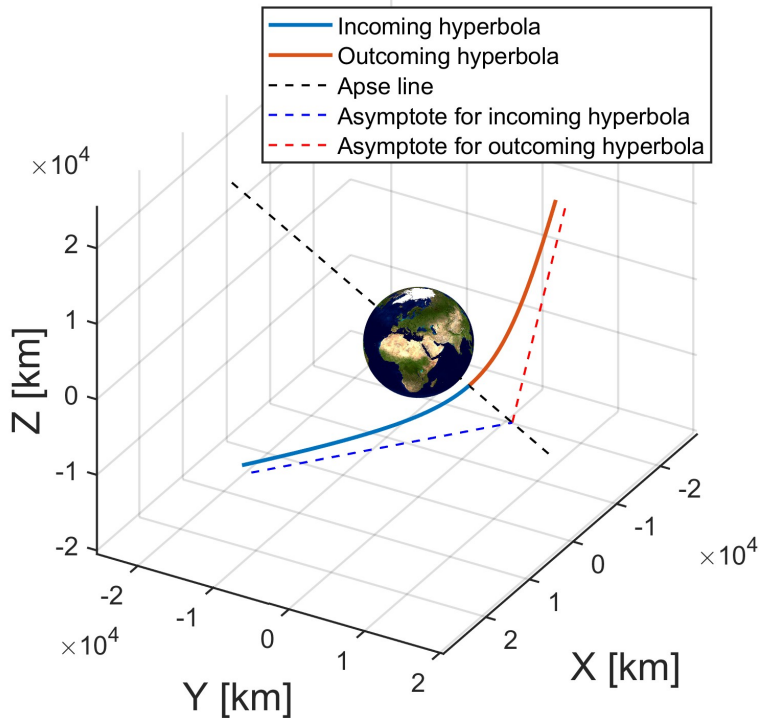


Figure 1.6: Gravity assist manoeuvre

2. Planetary mission

2.1. Introduction

The PoliMi Space Agency wants to launch a Planetary Explorer Mission, to perform Earth Observation. This section carries out relevant orbital analysis and groundtrack estimation while also considering two perturbation models. A modified groundtrack was proposed for a repeating groundtrack, and two propagation methods are used to perform the analysis which are then compared. A comparison between the real data of a satellite and its analytical results obtained with the code model is also performed for model validity.

2.1.1. Nominal Orbit

From the provided orbital parameters this satellite heavily contains geosynchronous orbital characteristics. Hence, the altitude at perigee is chosen as 35786 km^[4] - where it is possible to see the moon and J2 perturbation effect. Ω (right ascension of ascending node), ω (argument of perigee), and f_0 (initial true anomaly) are chosen arbitrarily for a simpler analysis.

a [km]	e [-]	i [deg]	Ω [deg]	ω [deg]	h_p [km]
42159	0.0007	32.5934	0	85	35786

Table 2.1: Keplerian elements of the orbit

The unperturbed nominal orbit is propagated as below in the Earth-centered reference frame:

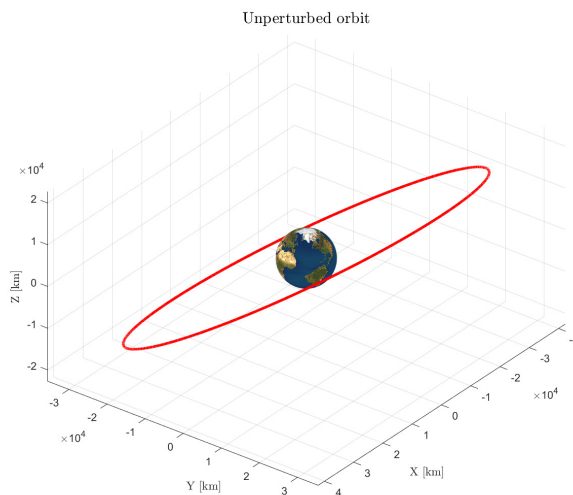


Figure 2.1: Assigned orbit

2.2. Groundtrack

The satellite's orbit is propagated to compute its groundtrack. The motion of the spacecraft is assumed to be a perturbed two body problem in Cartesian coordinates, described by the equation:

$$\dot{\mathbf{r}} = -\frac{\mu}{r^3} \mathbf{r} + \mathbf{a}_{\text{perturbation}} \quad (2.1)$$

This is solved using MATLAB's multi-step solver `ode113` function which is based on the Adams-Bashforth-Moulton method; it's chosen for its high accuracy over an extended period. A relative tolerance of 1×10^{-12} and absolute tolerance of 1×10^{-12} were selected for more precision.

2.2.1. Unperturbed Groundtrack

Nominal Orbit Groundtrack

The first required analysis of the ground track is for the nominal orbit considering an unperturbed case, where the $\mathbf{a}_{\text{perturbation}}$ in equation is null. The ground track was propagated for a period of 1 orbit of the satellite, 1 day and 10 days, as shown below.

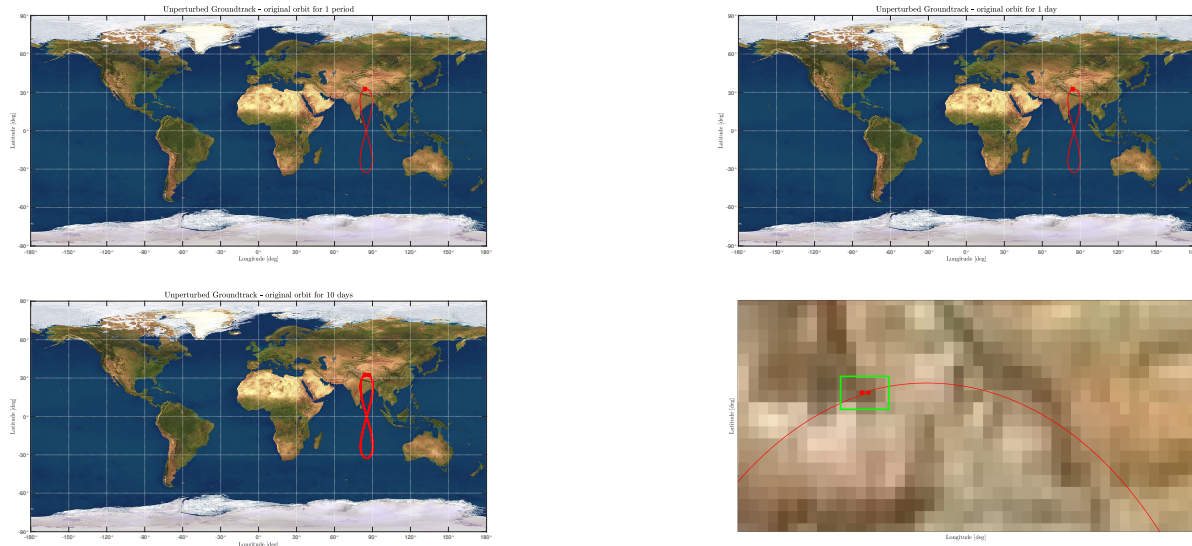


Figure 2.2: Ground track of the unperturbed nominal orbit during: (a) 1 orbit; (b) 1 day; (c) 10 days. Ground track path (—), Starting point (●), Ending point (■).

The groundtrack of this satellite has formed an “8” shape, a phenomenon known as the figure-eight groundtrack. At geosynchronous altitude, the location after one revolution is the same, and for geostationary orbits, the satellite always appears to be stationary over one location. The figure “8” occurs because the satellites relative velocity is less and greater, than locations on the Earth as it travels from the ascending node^[5].

Repeating Groundtrack

For establishing a good communication with the network of ground stations of PoliMi Space Agency, a repeating ground track with a ratio of 1:1 (for each orbit of the spacecraft, Earth has performed 1 revolution) is maintained. Therefore, the period of the repeating ground track orbit is computed. For an unperturbed orbit, the period is only a function of the semi-major axis and can be calculated to get the desired repeating ground track. Both equations are listed below. By extension, the other orbital parameters are kept the same as the nominal orbit.

$$T_{\text{repeating}} = \frac{1}{1} T_{\text{Earth}} \quad T = 2\pi \sqrt{\frac{a^3}{\mu}} \rightarrow a_{\text{repeating}} = 42166 \text{ km} \quad (2.2)$$



Figure 2.3: Ground track of the unperturbed repeating orbit during: (a) 1 orbit; (b) 4-k=4 orbits. Ground track path (—), Starting point (●), Ending point (■).

2.2.2. Perturbed Groundtrack

Assigned Perturbations

This project has been assigned with two perturbations: J_2 effect and Moon perturbation. J_2 effect consists of a perturbing potential on top of the central gravity field of the Earth. In order to model it, a zonal harmonic potential is used, function of the geocentric distance r and of the coelevation ϕ .

$$R(r, \phi) = \frac{\mu}{r} \left(-1 + \sum_{n=2}^{\infty} \left(\frac{R_E}{r} \right)^n J_n P_n(\cos \phi) \right) \quad (2.3)$$

Here, J_2 term is considered for modelling which is correlated to Earth oblateness. The perturbing acceleration due to J_2 effect is given as:

$$\mathbf{a}_{J_2} = \frac{3}{2} \frac{J_2 \mu R_E^2}{r^4} \left[\left(\frac{x}{r} \left(\frac{5z^2}{r^2} - 1 \right) \right) \mathbf{i} + \left(\frac{y}{r} \left(\frac{5z^2}{r^2} - 1 \right) \right) \mathbf{j} + \left(\frac{z}{r} \left(\frac{5z^2}{r^2} - 3 \right) \right) \mathbf{k} \right] \quad (2.4)$$

Perturbation due to the moon acting on the orbit is modelled through a two body problem scenario taking into account the force of the moon as a perturbing acceleration. This acceleration is computed from:

$$\mathbf{a}_{\text{Moon}} = \mu_{\text{Moon}} \left(\frac{\mathbf{r}_{m/s}}{r_{m/s}^3} - \frac{\mathbf{r}_m}{r_m^3} \right) \quad (2.5)$$

where $\mathbf{r}_{m/s}$ is the vector that goes from the S/C to the moon and \mathbf{r}_m is the vector that goes from Earth to Moon. Possible perturbations are charted in Figure 2.4. It is observed that the J_2 effect ($C_{2,0}$ in figure) and moon perturbation are one of the primary sources of orbital perturbation. Hence, our models and altitude choice are consistent.

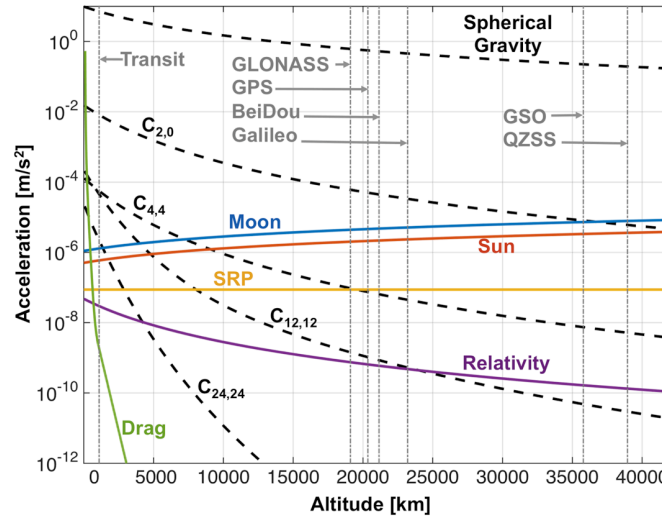
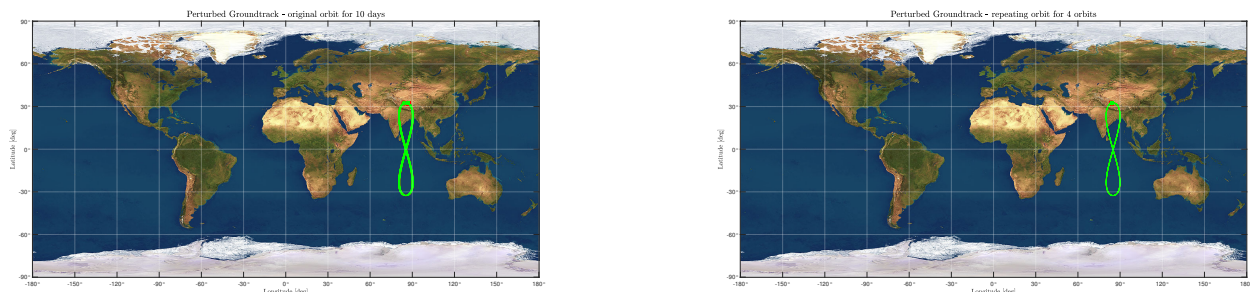


Figure 2.4: Orbit Perturbations from [6]

Nominal and Repeating Groundtrack



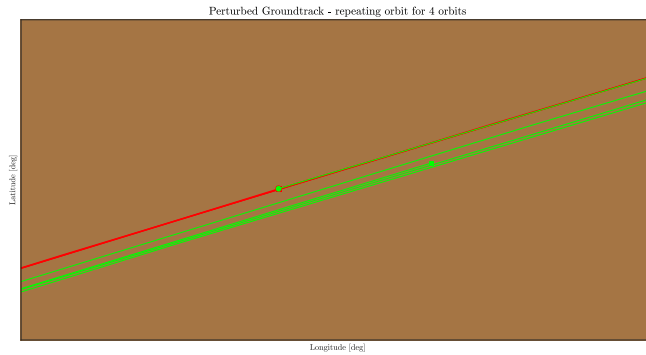


Figure 2.5: Ground track of the perturbed orbits: (a) Nominal orbit during 10 days; (b) Repeating orbit during 4 orbits; (c) Perturbation effect for repeating orbit. Ground track of unperturbed (—), Starting point (●), Ending point (■); Ground track of perturbed (—), Starting point (●), Ending point (■).

It is observed that the perturbations have a great impact on the ground track path of the satellite. Both the nominal and repeating orbits get out of phase with relation to the unperturbed case. From Figure 2.5, the repeating ground track orbit proposed does not work in the presence of assigned perturbations.

2.3. Orbit Propagation

Orbits were propagated using Cartesian coordinates (Newton's equations of motion), or Keplerian elements (Gauss' planetary equations). Gauss' equations are presented in the Radial-Transversal-Out-of-plane reference frame (RSW). All formulas can be found in [7].

$$\begin{aligned}
 \frac{da}{dt} &= \frac{2a^2}{h} \left(e \sin f a_r + \frac{p}{r} a_s \right) \\
 \frac{de}{dt} &= \frac{1}{h} (p \sin f a_r + ((p+r) \cos f + r e) a_s) \\
 \frac{di}{dt} &= \frac{r \cos(f+\omega)}{h} a_w \\
 \frac{d\Omega}{dt} &= \frac{r \sin(f+\omega)}{h \sin i} a_w \\
 \frac{d\omega}{dt} &= \frac{1}{he} (-p \cos f a_r + (p+r) \sin f a_s) - \frac{r \sin(f+\omega) \cos i}{h \sin i} a_w \\
 \frac{df}{dt} &= \frac{h}{r^2} + \frac{1}{eh} (p \cos f a_r - (p+r) \sin f a_s)
 \end{aligned} \tag{2.6}$$

For the moon perturbation, which cannot be directly expressed in RSW frame, it's possible to transform the perturbing accelerations from Cartesian to RSW. The three rotation matrices for this are shown below where a rotation of Ω around the third axis of the inertial frame is performed, then a rotation of i around the first axis of the rotated frame, and finally a rotation of an angle $\theta + \omega$ around the third axis of the last frame.

$$R_\Omega = \begin{bmatrix} \cos \Omega & \sin \Omega & 0 \\ -\sin \Omega & \cos \Omega & 0 \\ 0 & 0 & 1 \end{bmatrix}; \quad R_i = \begin{bmatrix} 1 & 0 & 0 \\ 0 & \cos i & \sin i \\ 0 & -\sin i & \cos i \end{bmatrix}; \quad R_{\theta+\omega} = \begin{bmatrix} \cos(\theta+\omega) & \sin(\theta+\omega) & 0 \\ -\sin(\theta+\omega) & \cos(\theta+\omega) & 0 \\ 0 & 0 & 1 \end{bmatrix} \tag{2.7}$$

2.3.1. History of the Keplerian Elements

The Keplerian elements were obtained through the integration of the equation of motion and of the Gauss planetary equations. The propagation time is taken as 10 years, so it's sufficient to see the perturbations properly developed for this project's case. The evolution of the data and of the relative error between both methods of integration are presented below:

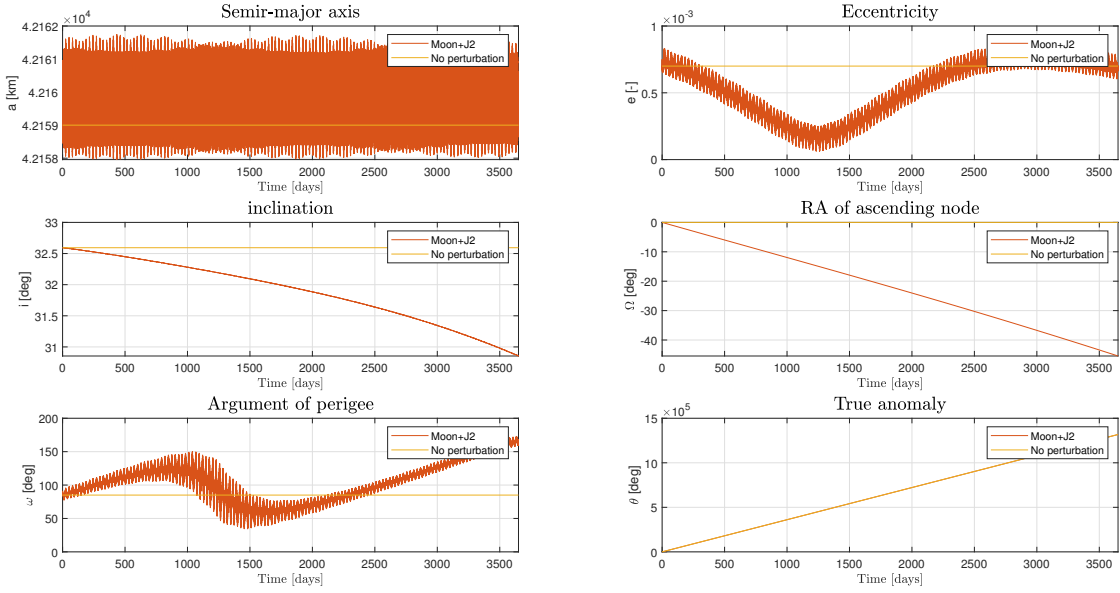


Figure 2.6: Evolution of the data

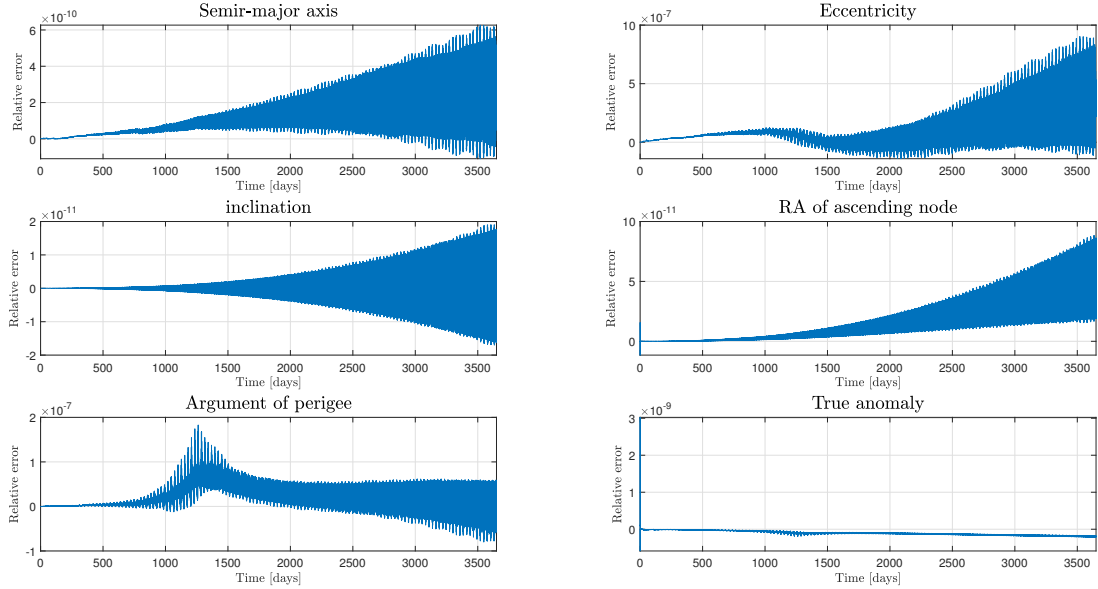


Figure 2.7: Relative error between both methods of integration

It is possible to distinguish a long-periodic behaviour and a short-periodic behaviour by looking at the evolution of orbital elements. It is very clear for eccentricity e , inclination i , and also for argument of perigee ω to a sufficient extent. Semi-major axis presents both short-periodic and long-periodic behaviour. As for the right ascension of ascending node Ω , and true anomaly f , the short-periodic behaviour is less visible but still present. From Figure 2.7 of relative error between Gauss' resolution and Cartesian resolution, it can be observed that the two methods are equivalent if the precision of the two is compared.

2.3.2. Representation of the Evolution of the Orbit



Figure 2.8: Orbit evolution representation in the 3D plane. Colors are used in order to let the reader understand the evolution of the orbit: in chronological order there are (—), (—), (—), (—), (—), (—), (—), and (—). The initial position of spacecraft is (*) and the final position of spacecraft is (*).

2.3.3. Filtering

The filtering of the results is now performed using the *movemean* function to see how the perturbations generate behaviours with different frequencies, and to retrieve the long-period and the secular evolution of the data. A period of 6 months has been chosen to for better visualization.

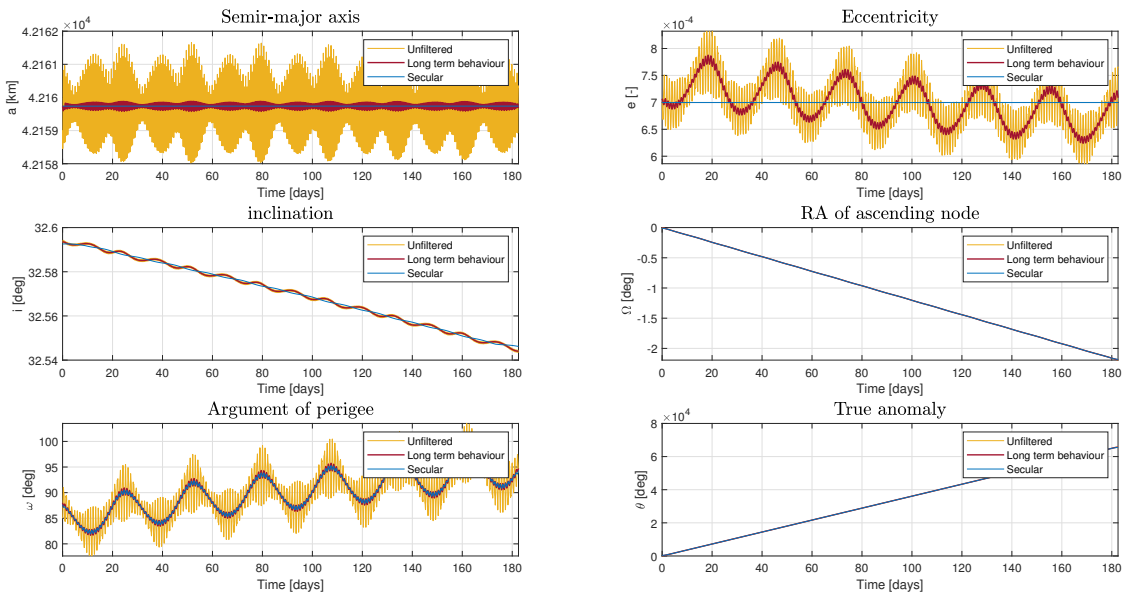


Figure 2.9: Orbit Perturbations

Here, long-periodic behaviour is related to moon perturbation and short-periodic perturbation is related to J2 effect. This is due to the fact that the J2 perturbation is related to the oblateness of the Earth and of the S/C's orbit, whose period is much lower than the Moon orbit period. Two different filters are used: the filter used to remove short-term behaviour has a cut-off frequency of 100 days^{-1} , instead, the filter used to remove long-term behaviour has a cut-off frequency of 1 days^{-1} .

2.4. Comparison with Real Data

To evaluate the precision of the methods used for the assignment, the models were compared with real data of the payload SDO, NORAD Catalogue Number 36395, from [8][9]. This choice was motivated because the payload's orbit is similar to the nominal orbit of the assignment. The altitude of the orbit is also in the GSO region, which means the J2 effect and Moon disturbances are very prominent in the region. It is also important to note that a payload will

correct its orbit using active propulsion. As the numerical model does not consider this kind of manoeuvres, a worse coincidence between results is expected. To compute the orbit propagation, the initial orbital elements were those collected from Space-Track at the initial time, shown on the table. To propagate the orbit, Gauss' planetary equations in RSW frame were solved numerically using ode113. A low-pass filter of frequency 0.4949day^{-1} was used to get the mean value every two orbits, considering the initial period. Filtering was done using $N = \lceil \frac{T_{cut}}{\Delta t} \rceil$. T_{cut} is the period of the oscillation to discard and Δt is the time step of the propagation.

a [km]	e [-]	i [deg]	Ω [deg]	ω [deg]	h_p [km]
42165.38456	0.000069	27.833	169.5864	245.7244	35783.9

Table 2.2: Keplerian elements of orbit

From the figures below, it can be observed that the numerical approach is capable of estimating the orbit with good reliability as the trends of both results are very similar. The differences seen on each plot were expected, as only J2 and Moon perturbations were taken into account for the numerical model. There's a great difference in the short-term behaviour between numerical simulation and the real data. As the numerical simulation can generate data for any time interval, it can evaluate the short-term oscillations, while the real data is measured with a broader list of other elements that can change the values of the Keplerian data.

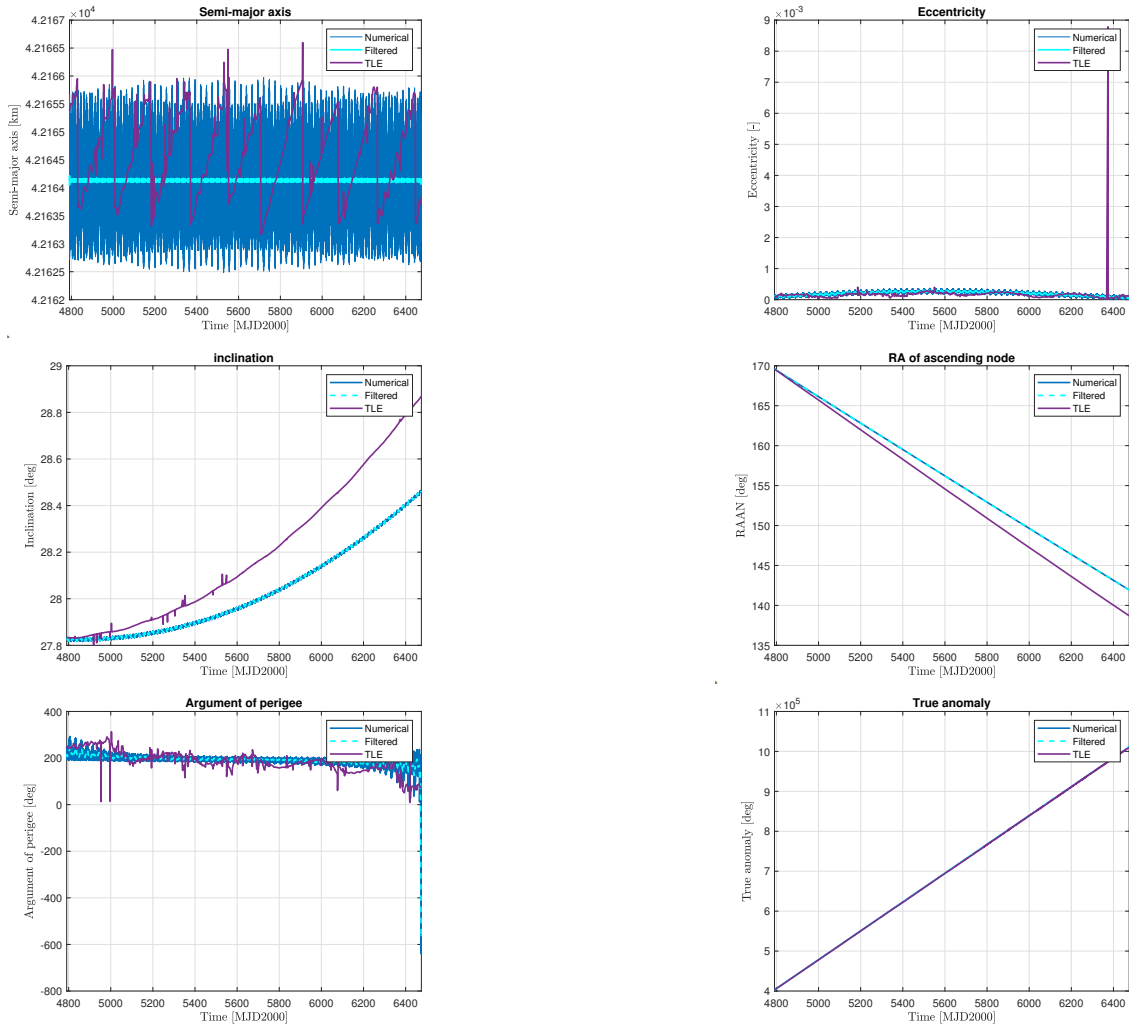


Figure 2.10: Numerical, filtered and TLE data

Bibliography

- [1] Davide Menzio. Grid-search applications for trajectory design in presence of flybys. PhD Dissertation, 2019. Site: <https://www.politesi.polimi.it/handle/10589/152568>.
- [2] Richard Battin. *An introduction to the mathematics and methods of astrodynamics*. AIAA Education Series, 1987.
- [3] Gianmarco Radice Pierluigi Di Lizia. Advanced global optimisation tools for mission analysis and design. Paper, 2004. Site: https://www.esa.int/gsp/ACT/resources/act_papers.
- [4] ESA. Altitude at perigee for geo. Website, 2020. Site: https://www.esa.int/ESA_Multimedia/Images/2020/03/Geostationary_orbit.
- [5] David A. Vallado. *Fundamentals of Astrodynamics and Applications*. Microcosm Press and Springer, 2013.
- [6] T. G. R. Reid. Orbital diversity for global navigation satellite systems. Stanford University, 2017. Site: https://www.researchgate.net/publication/323245224_Orbital_Diversity_for_Global_Navigation_Satellite_Systems.
- [7] Howard D. Curtis. *Orbital Mechanics for Engineering Students*. Elsevier, 2014.
- [8] Space Track. Tles data. Website, 2024. Site: <https://www.space-track.org/auth/login>.
- [9] N2YO. Details on compared mission sto. Website, 2024. Site: <https://www.n2yo.com/satellite/?s=36395>.